

## THE ACCELERATION MECHANISM OF RESISTIVE MAGNETOHYDRODYNAMIC JETS LAUNCHED FROM ACCRETION DISKS

TAKUHITO KUWABARA

Space Simulation Group, Applied Research and Standards Department, National Institute of Information and Communications Technology,  
4-2-1 Nukui-Kitamachi, Koganei, Tokyo 184-8795, Japan; kuwabrtk@cc.nao.ac.jp

KAZUNARI SHIBATA

Kwasan and Hida Observatories, Kyoto University, Yamashina, Kyoto 607-8471, Japan; shibata@kwasan.kyoto-u.ac.jp

TAKAHIRO KUDOH

Department of Physics and Astronomy, University of Western Ontario, London, ON N6A 3K7, Canada; kudoh@astro.uwo.ca

AND

RYOJI MATSUMOTO

Department of Physics, Faculty of Science, Chiba University, Inage-ku, Chiba 263-8522, Japan; matumoto@astro.s.chiba-u.ac.jp

Received 2003 August 12; accepted 2004 November 22

### ABSTRACT

We analyzed the results of nonlinear resistive magnetohydrodynamic (MHD) simulations of jet formation to study the acceleration mechanism of axisymmetric, resistive MHD jets. The initial state is a constant angular momentum, polytropic torus threaded by weak uniform vertical magnetic fields. The time evolution of the torus is simulated by applying the CIP-MOCCT scheme extended for resistive MHD equations. We carried out simulations up to 50 rotation periods at the innermost radius of the disk created by accretion from the torus. The acceleration forces and the characteristics of resistive jets were studied by computing forces acting on Lagrangian test particles. Since the angle between the rotation axis of the disk and magnetic field lines is smaller in resistive models than in ideal MHD models, magnetocentrifugal acceleration is smaller. The effective potential along a magnetic field line has a maximum around  $z \sim 0.5r_0$  in resistive models, where  $r_0$  is the radius at which the density of the initial torus is maximum. Jets are launched after the disk material is lifted to this height by pressure gradient force. Even in this case, the main acceleration force around the slow magnetosonic point is the magnetocentrifugal force. The power of the resistive MHD jet is comparable to the mechanical energy liberated in the disk by mass accretion. Joule heating is not essential for the formation of jets.

*Subject headings:* accretion, accretion disks — diffusion — galaxies: jets — ISM: jets and outflows — methods: numerical — MHD

### 1. INTRODUCTION

Magnetically driven mass outflows from accretion disks have been studied extensively. Blandford & Payne (1982) showed that a magnetocentrifugally driven cold outflow emanates from an accretion disk when the angle  $\theta$  between poloidal magnetic field lines threading the disk and the rotation axis of the disk is larger than  $30^\circ$ . Nonlinear magnetohydrodynamic (MHD) simulations of jet formation including accretion disks were first carried out by Uchida & Shibata (1985) and Shibata & Uchida (1986). Since the magnetically driven jet extracts angular momentum from the disk, the jet formation process enhances the accretion of the disk material. The back reaction of the jet formation on disk accretion and its relation to the magnetorotational instability (MRI; Balbus & Hawley 1991) were discussed by Stone & Norman (1994), Matsumoto et al. (1996), and Kudoh et al. (2002).

A key question that is often raised with regards to the time-dependent simulations of jet formation is whether the system approaches a steady state. Axisymmetric ideal MHD simulations of jet formation including an accretion disk show episodic outflows instead of approaching a quasi-steady state (e.g., Kuwabara et al. 2000). One successful approach to get a steady jet by non-steady simulations is to treat the disk as a time-independent boundary condition (e.g., Ustyugova et al. 1995; Romanova et al.

1997; Ouyed & Pudritz 1997; see Fendt & Čemeljić 2002 for resistive MHD simulations). Another approach is to include an accretion disk inside the computational box and assume magnetic diffusivity (Kuwabara et al. 2000; Casse & Keppens 2002, 2004).

Kuwabara et al. (2000) carried out 2.5-dimensional axisymmetric resistive MHD simulations starting from a rotating torus initially threaded by weak uniform vertical magnetic fields. They showed that the jet property drastically changes depending on the magnetic diffusivity, which they assumed to be uniform. When the magnetic diffusivity is small, mass accretion and jet formation take place intermittently. On the other hand, in mildly diffusive disks they showed by simulations for a timescale of about 50 rotation periods at the innermost radius of the disk that both jets and accretion disks approach a quasi-steady state. Casse & Keppens (2002, 2004) extended this study to the case of a geometrically thin disk initially threaded by equipartition ( $\beta = P_{\text{gas}}/P_{\text{mag}} \sim 1$ ) poloidal magnetic fields. By carrying out simulations assuming magnetic diffusivity localized inside the disk, they achieved a near-stationary state.

In order to study the acceleration mechanisms and energy transport of resistive MHD jets more quantitatively, we re-computed the simulation models adopted by Kuwabara et al. (2000) by applying the CIP-MOCCT scheme (Kudoh et al. 1998), which is more robust and accurate than the scheme we adopted in Kuwabara et al. (2000).

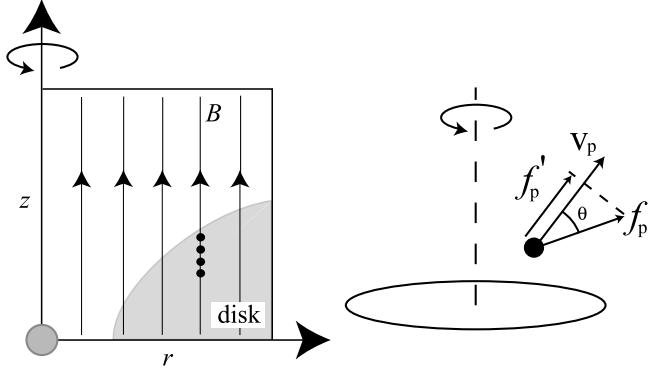


Fig. 1.—*Left*: Lagrangian test particles initially located near the surface of the accretion disk along a magnetic field line. *Right*: Schematic picture showing how to extract the force along the streamline.

In § 2, we describe the assumptions and numerical methods. Numerical results are presented in § 3. Discussions and conclusions are given in § 4.

## 2. MODELS

### 2.1. Assumptions and Basic Equations

We solve two-dimensional nonlinear, time-dependent, compressible resistive MHD equations in a cylindrical coordinate system \$(r, z)\$ under the assumption of axisymmetry to investigate the jet ejection from the accretion disk. The \$z\$-direction is parallel to the rotational axis of the accretion disk (see Fig. 1). The basic equations are

$$\frac{\partial \rho}{\partial t} + \mathbf{V} \cdot \nabla \rho = -\rho \nabla \cdot \mathbf{V}, \quad (1)$$

$$\frac{\partial \mathbf{V}}{\partial t} + \mathbf{V} \cdot \nabla \mathbf{V} = -\frac{1}{\rho} \nabla P + \frac{1}{4\pi\rho} (\nabla \times \mathbf{B}) \mathbf{B} - \nabla \psi, \quad (2)$$

$$\frac{\partial \mathbf{B}}{\partial t} = \nabla (\mathbf{V} \times \mathbf{B} - \eta \nabla \times \mathbf{B}), \quad (3)$$

$$\frac{\partial P}{\partial t} + \mathbf{V} \cdot \nabla P = -\gamma P \nabla \cdot \mathbf{V} + (\gamma - 1) \frac{\eta'}{4\pi} (\nabla \times \mathbf{B})^2, \quad (4)$$

where \$\psi\$ is the gravitational potential

$$\psi = -\frac{GM}{(r^2 + z^2)^{1/2}}, \quad (5)$$

\$G\$ is the gravitational constant, \$M\$ is the mass of the central object, and \$\eta\$ is the resistivity, which is assumed to be uniform. The other symbols have their usual meanings. In equation (4), we set \$\eta' = \eta\$ or 0. The latter corresponds to the case in which we neglect Joule heating (or equivalently, we assume cooling that balances with the Joule heating). The units of length, velocity, time, and density are \$r\_0\$, \$V\_{K0}\$, \$r\_0/V\_{K0}\$, and \$\rho\_0\$, where \$r\_0\$ is the radius at which the density of the torus is maximum, and \$V\_{K0}\$ and \$\rho\_0\$ are the Keplerian rotation speed and the density at \$(r, z) = (r\_0, 0)\$, respectively. In this normalization, we have two nondimensional parameters,

$$E_{\text{th}} = \frac{V_{s0}^2}{\gamma V_{K0}^2}, \quad (6)$$

$$E_{\text{mg}} = \frac{V_{A0}^2}{V_{K0}^2}, \quad (7)$$

where \$V\_{s0} = (\gamma P\_0/\rho\_0)^{1/2}\$ and \$V\_{A0} = [B\_0^2/(4\pi\rho\_0)]^{1/2}\$ are the sound speed and Alfvén speed at \$(r\_0, 0)\$, respectively. Here, \$E\_{\text{th}}\$ is the ratio of thermal energy to gravitational energy and \$E\_{\text{mg}}\$ is the ratio of magnetic energy to gravitational energy. The normalized resistivity \$\bar{\eta}\$ is defined as \$\bar{\eta} = \eta/(r\_0 V\_{K0})\$ and the magnetic Reynolds number at \$(r\_0, 0)\$ is defined as \$R\_{m0} \equiv r\_0 V\_{A0}/\eta\$.

### 2.2. Initial Condition

We assume an equilibrium disk rotating around a central object surrounded by a hot corona (e.g., Matsumoto et al. 1996). The assumption of the existence of a hot corona is a natural consequence of energy transfer from magnetically active disks. Such a corona exists above galactic gas disks and the solar photosphere (see, e.g., Galeev et al. 1981 for accretion disk corona). Equilibrium solutions of a torus can be obtained under the following simplifying assumptions. Here we adopted the Newtonian analogue of Abramowicz's relativistic tori (Abramowicz et al. 1978). The distribution of angular momentum is

$$L = L_0 r^a. \quad (8)$$

We assume a polytropic equation of state,

$$P = K \rho^{1+1/n}. \quad (9)$$

The density distribution of the torus is determined by

$$-\frac{GM}{(r^2 + z^2)^{1/2}} + \frac{1}{2(1-a)} L_0^2 r^{2a-2} + (n+1) \frac{P}{\rho} = \text{constant}. \quad (10)$$

The mass distribution outside the torus is assumed to be that of the isothermal nonrotating high-temperature halo surrounding the central object,

$$\rho = \rho_h \exp\left\{\alpha \left[\frac{r_0}{(r^2 + z^2)^{1/2}} - 1\right]\right\}, \quad (11)$$

where \$\alpha = \gamma V\_{K0}^2/V\_{sc}^2\$. Here \$V\_{sc}\$ and \$\rho\_h\$ are the sound velocity and density in the halo at \$(0, r\_0)\$, respectively. We assume that \$a = 0\$ (\$L = \text{constant}\$), \$n = 3\$, \$\gamma = 5/3\$, \$\alpha = 1.0\$, \$\rho\_h/\rho\_0 = 10^{-3}\$, \$E\_{\text{th}} = 5.0 \times 10^{-2}\$, and \$E\_{\text{mg}} = 5.0 \times 10^{-4}\$. The initial magnetic field is assumed to be uniform and parallel to the \$z\$-axis.

The magnetic Reynolds number is defined by \$R\_m = \lambda V\_A/\eta = R\_{m0}(\lambda/r\_0)(V\_A/V\_{A0})\$, where \$\lambda = 2\pi V\_A/\Omega\$ is the characteristic scale of the magnetorotational instability, \$V\_A\$ is the Alfvén velocity, and \$\Omega\$ is the angular velocity of the disk. It increases from inside the torus to the halo and it becomes \$R\_m \gg 1\$ in the halo; thus, magnetic diffusion is not important there (Kuwabara et al. 2000).

### 2.3. Numerical Methods and Boundary Conditions

We solved equations (1)–(4) by using the CIP-MOCCT method. The algorithm of the original CIP-MOCCT method and results of test simulations are described in Kudoh et al. (1998, 1999). In this method, the CIP scheme (Yabe & Aoki 1991) is used for the hydrodynamic part and the MOCCT scheme (Stone & Norman 1992) is used to solve the induction equation (3) and to evaluate the Lorentz force terms. The basic equations (1), (2), and (4) are expressed in nonconservation form as

$$\frac{\partial f}{\partial t} + (\mathbf{V} \cdot \nabla) f = S, \quad (12)$$

TABLE 1  
MODEL PARAMETERS

Model	$\bar{\eta}$	$R_{m0}$	Outflow Type	Joule Heating in Energy Equation
I.....	0.0	$\infty$	Episodic	no
R.....	$1.25 \times 10^{-2}$	1.8	Quasi steady	yes
RC.....	$1.25 \times 10^{-2}$	1.8	Quasi steady	no

NOTES.—In all models,  $E_{\text{th}} = V_{s0}^2/(\gamma V_{K0}^2) = 5 \times 10^{-2}$ ,  $E_{\text{mg}} = V_{A0}^2/V_{K0}^2 = 5 \times 10^{-4}$ , and  $\rho_h/\rho_0 = 10^{-3}$ .

where  $S$  is the source term. We solve the equation in two steps; the advective step  $\partial f/\partial t + (\mathbf{V} \cdot \nabla)f = 0$  and the source step  $\partial f/\partial t = S$ . We revised the source step to ensure higher accuracy in space and time. In the MOCCT step, we modified the original scheme such that we include the resistive term in the induction equation and the characteristic equations of Alfvén waves are solved using the CIP scheme.

The size of the simulation box is  $(r_{\text{max}} \times z_{\text{max}}) = (5.1r_0 \times 13.4r_0)$ , the number of grid points is  $(N_r, N_z) = (200, 256)$ , and the grid size is  $\Delta r = 0.01r_0$  when  $0 \leq r \leq 1$  and  $\Delta z = 0.01r_0$  when  $0 \leq z \leq 1$ . Otherwise, the grid size increases with  $r$  and  $z$ . At  $r = 0$ , we assume that  $\rho, P, V_z$ , and  $B_z$  are symmetric, while  $V_r, V_\phi, B_r$ , and  $B_\phi$  are antisymmetric. We computed only the upper half-plane ( $z > 0$ ) by assuming that  $\rho, P, V_r, V_\phi$ , and  $B_z$  are symmetric, while  $V_z, B_r$ , and  $B_\phi$  are antisymmetric with respect to  $z = 0$ . The outer boundaries at  $r = r_{\text{max}}$  and  $z = z_{\text{max}}$  are free boundaries where waves can be transmitted. We softened the gravitational potential inside  $R = (r^2 + z^2)^{1/2} = R_{\text{in}} = 0.2r_0$  to avoid the singularity at  $R = 0$ . As we show later, the disk material smoothly penetrates into the region  $R < R_{\text{in}}$ .  $R_{\text{in}}$  can be considered as the innermost radius of the disk. The unit time  $t_0 = r_0/V_{K0} \sim 11R_{\text{in}}/V_{K,\text{in}}$ , where  $V_{K,\text{in}}$  is the Keplerian rotation speed at  $r = R_{\text{in}}$ , corresponds to 1.8 rotation periods at  $r = R_{\text{in}}$ .

We analyzed the results of three simulations (see Table 1). Model R is a mildly diffusive model ( $\bar{\eta} = \bar{\eta}' = 1.25 \times 10^{-2}$ ). Model RC is the resistive model without Joule heating ( $\bar{\eta} = 1.25 \times 10^{-2}$ ,  $\bar{\eta}' = 0$ ). Model I is the nondiffusive model ( $\bar{\eta} = \bar{\eta}' = 0$ ). Model R and model I are the same as those reported by Kuwabara et al. (2000).

To study the acceleration mechanism of the jet, we put Lagrangian test particles near the disk surface and computed the time evolutions of the location of these particles and evaluated the forces acting on each particle as schematically shown in Figure 1 (*left*). The initial positions of particles are selected such that they form the main part of the jet. In model R, we put Lagrangian particles on a magnetic field line at  $r = 1.5r_0$ , between  $z = 0.64r_0$  and  $0.84r_0$ . In model I, we put them on a magnetic field line at  $r = 0.8r_0$ , between  $z = 0.31r_0$  and  $0.46r_0$ . The particle positions are updated by using fluid velocity  $\mathbf{V} = (V_r, V_z)$  as follows:  $r_p^{n+1} = r_p^n + V_r \Delta t$ ,  $z_p^{n+1} = z_p^n + V_z \Delta t$ . Here  $r_p$  and  $z_p$  are the position of particles and  $n + 1$  and  $n$  show the time step whose interval is  $\Delta t$ . In Figure 1 (*right*), we schematically show the force  $f_p'$ , defined as the projection of poloidal force per mass  $\mathbf{f}_p$  to the direction of poloidal velocity vector  $\mathbf{V}_p$  of the particle,

$$f_p' = |\mathbf{f}_p| \frac{\mathbf{f}_p \cdot \mathbf{V}_p}{|\mathbf{f}_p| |\mathbf{V}_p|}. \quad (13)$$

When the sign of force  $f_p'$  is positive, the force accelerates the particle. On the other hand, when the sign of the force  $f_p'$  is

negative, it decelerates the particle, respectively. By plotting the time variation of  $f_p'$ , we can check the acceleration force along the streamline acting on particles.

### 3. NUMERICAL RESULTS

#### 3.1. Time Evolution of Jets

Figure 2 (*top panels*) shows the time evolution of temperature distribution (*color scale*), magnetic field lines (*white curves*), and velocity vectors (*arrows*) in model R. Numerical results are in good agreement with those reported by Kuwabara et al. (2000). As Kudoh et al. (1998) have already shown, numerical results obtained by the CIP-MOCCT scheme agree well with those obtained by the modified Lax-Wendroff scheme with artificial viscosity, except that numerical oscillations in low- $\beta$  regions are not prominent when the CIP-MOCCT method is used and that contact surfaces are sharply traced with the CIP-MOCCT method. Figure 2 (*bottom panels*) show the time evolution of model RC. In this model, resistivity is included in the induction equation but the Joule heating term is not included in the energy equation. Numerical results indicate that Joule heating is not essential for jet formation. The collimation of the jet is better in the model without Joule heating (model RC) because the temperature of the jet is lower than that in the model with Joule heating (model R).

Figure 3 (*left*) shows the density distribution at  $t = 25$ . A high-density ridge is formed near the outermost radius of the initial torus. This ridge is the contact surface between the disk material ejected from the disk and the ambient halo. The main part of the jet is inside this dense ridge. The density of the main part of the jet at  $z = 4r_0$  is  $\rho_{\text{jet}} \sim 10^{-3} \rho_0$ , but still larger than the halo density. Figure 3 (*right*) shows the volume-rendered image of the density distribution (*color scale*) and the three-dimensional structure of magnetic field lines (*solid curves*). The magnetic field lines are highly twisted owing to the rotation of the disk.

#### 3.2. Acceleration Force of Jets

Figure 4 shows the distribution of gas pressure (*gray scale*), magnetic field lines (*white curves*), and velocity vectors for model I (*left*), model R (*middle*), and model RC (*right*). In the ideal MHD model (model I), gas pressure is small in the inner region ( $0.2 < r < 0.7$  and  $0 < z < 0.1$ ), where magnetic pressure supports the disk. Mass accretion proceeds along the surface channel where the angular momentum of the infalling gas is magnetically extracted. Since the magnetic fields are frozen to the plasma, mass accretion deforms the magnetic field lines. Magnetocentrifugal force accelerates the plasma along magnetic field lines that are at a sufficiently large angle from the rotation axis.

In resistive models (model R and model RC), magnetic field lines are not deformed so much as those in the ideal MHD model because matter can traverse the magnetic field lines. Since the infalling matter loses less angular momentum than that in the ideal MHD model, a centrifugally supported inner disk is formed. Because of adiabatic compression, gas pressure increases in the equatorial region. Gas pressure in the surface region of the disk is larger in model R than in model RC because of Joule heating.

Figure 5 (*right*) shows the dependence of the inclination angle  $\theta$  on the poloidal magnetic field line in model R, depicted by a white curve in the left panel. The angle from the rotation axis of the disk does not exceed  $30^\circ$ . This does not indicate that magnetocentrifugal acceleration is unimportant because fluid elements away from the equatorial plane can be accelerated by the magnetocentrifugal force even when  $\theta < 30^\circ$ .

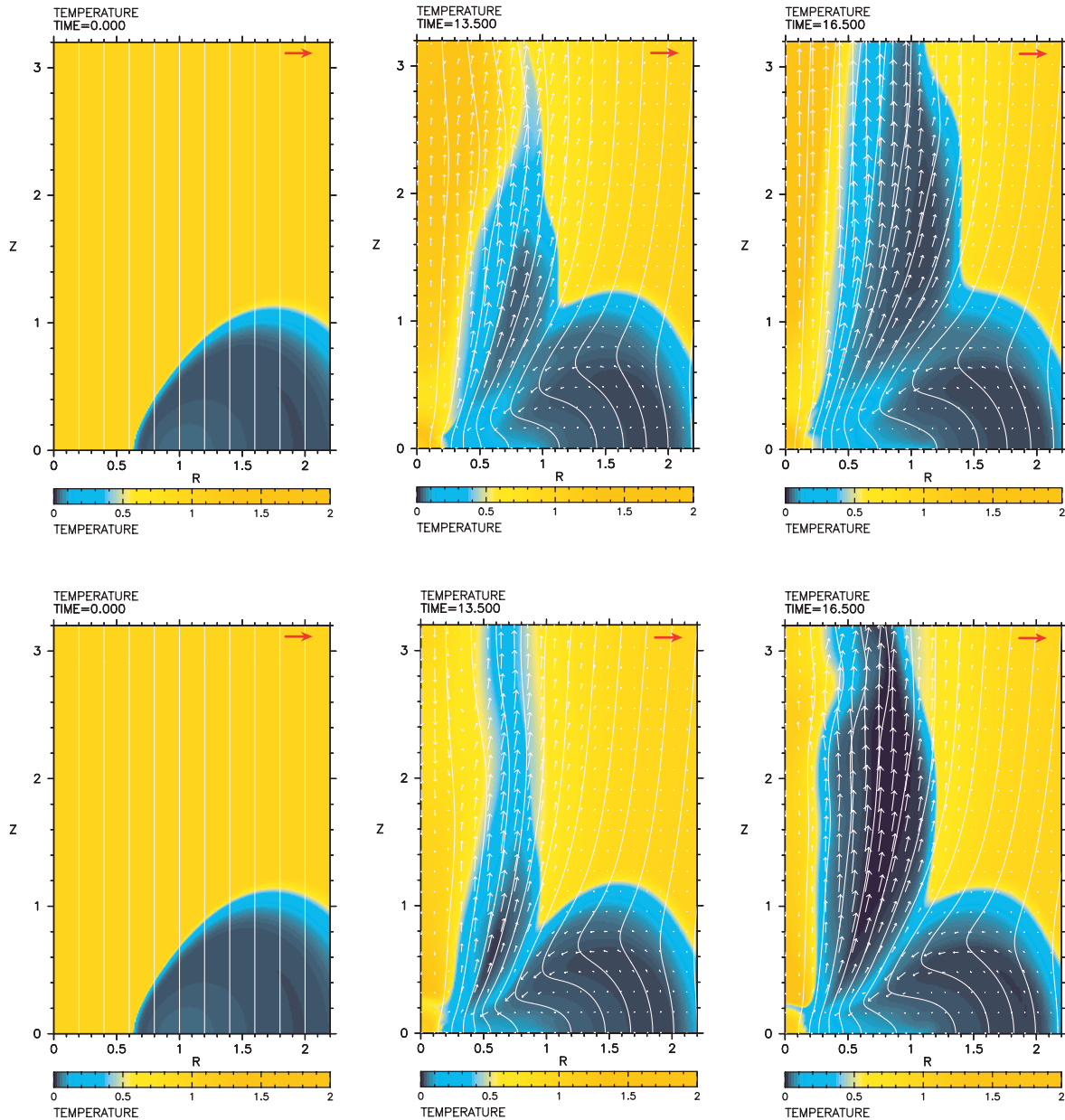


FIG. 2.—Time evolution of temperature distribution (*color contours*), magnetic field lines (*white curves*), and velocity vectors (*white arrows*). *Top panels*: Model R (with Joule heating). *Bottom panels*: Model RC (without Joule heating).

Figure 6 (*left*) shows the isocontours of temperature (*gray-scale contour*), magnetic field lines (*white curves*), and velocity vectors (*arrows*) for model R at  $t = 13.1$ . Cold disk matter is accelerated along the magnetic field lines and forms jets as we already showed in Kuwabara et al. (2000). Figure 6 (*right*) shows the distribution of pressure (*gray-scale contour*), poloidal stream lines (*white curves*), and poloidal Lorentz force vectors  $(\mathbf{J} \times \mathbf{B})_p / \rho = [(\mathbf{J} \times \mathbf{B})_r, (\mathbf{J} \times \mathbf{B})_z] / \rho$  (*arrows*), where  $\mathbf{J} = c\nabla \times \mathbf{B} / (4\pi)$ . The softened gravitational potential inside  $r = R_{\text{in}}$  has a small influence on the formation of jets emanating from the outer radius. The streamlines shown in Figure 6 (*right*) smoothly pass through  $R = R_{\text{in}}$  and slowly accrete to the central object.

The poloidal Lorentz force is almost perpendicular to the poloidal stream lines in the launching region of the jet. This means that Lorentz force collimates the outflow toward the rotation axis, but acceleration along the poloidal magnetic

field lines is small. We would like to point out that inside the disk, the poloidal Lorentz force points toward the equatorial plane because the magnetic field mainly has a  $+\phi$  component and the electric current mainly has a  $-r$  component. Thus, the Lorentz force compresses the torus in the vertical direction. This force suppresses the outflow from this region. However, in the surface layer of the disk, where the magnetic field lines change their direction from radial to vertical, the poloidal Lorentz force changes its direction and enables outflows.

A black circle in Figure 6 (*right*) denotes the position of the test particle initially inside the torus at  $(r, z) = (1.5r_0, 0.73r_0)$  and later accelerated along the magnetic field line. For this test particle, the poloidal Lorentz force makes almost no contribution to the acceleration along the magnetic field line until  $t \sim 13.0$ . On the other hand, the test particle is in the region where pressure gradient force lifts the particle in the vertical direction.

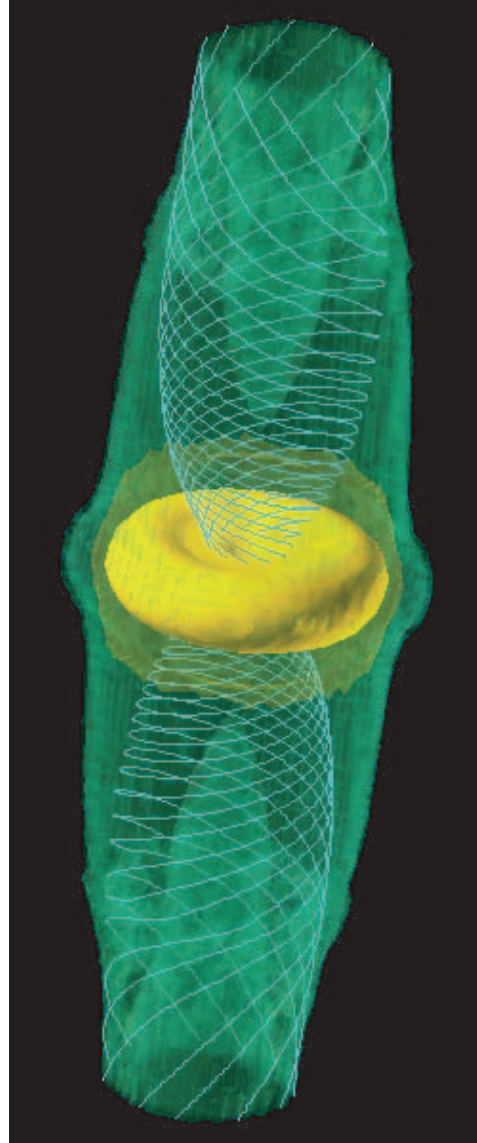
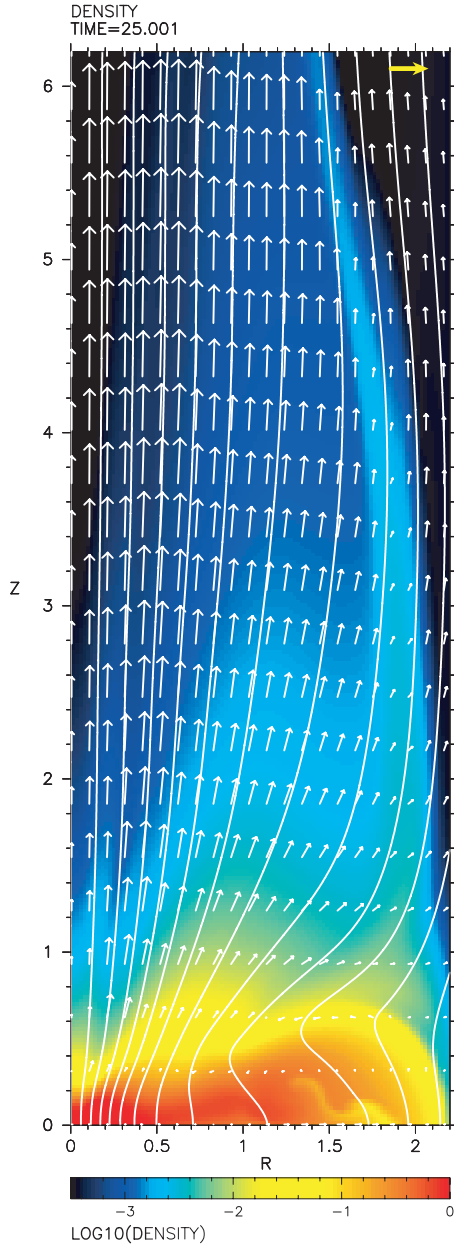


FIG. 3.—*Left*: Density distribution (color contours), velocity vectors (white arrows), and magnetic field lines (white curves) at  $t = 25$ . The yellow arrow shows the unit velocity. *Right*: Three-dimensional distribution of density (color) and magnetic field lines (blue curves).

Figure 7 (*left*) shows the trajectories of the Lagrangian particles that are initially on a magnetic field line at  $r = 1.5r_0$  in model R. The initial position of particles is selected such that they form the main part of the jet. Figure 7 (*right*) shows the time variation of the forces per mass along the streamline exerted on the particle, which is shown by open circles in Figure 7 (*left*). The forces accelerate the particle along its stream line when the sign is positive and decelerate the particle when the sign is negative. In Figure 7 (*right*), the curve  $F_c$  shows the centrifugal force  $(v_\phi^2/r)_\parallel$ , the curve  $F_g$  shows the gravity  $(-GM/r^2)_\parallel$ , the curve  $F_p$  shows the pressure gradient force  $(-\nabla P)_\parallel/\rho$ , the curve  $F_L$  shows the poloidal Lorentz force per mass  $(\mathbf{J} \times \mathbf{B})_{p\parallel}/\rho$ , and the curve  $F_t$  shows the total force per mass obtained by summing the four forces. Here the subscript “ $\parallel$ ” means the component parallel or antiparallel to the direction of the velocity vector of the particle. The two vertical dotted lines show the time when  $V_z$  changes from negative to positive (*left line*) and when  $V_r$

changes from negative to positive (*right line*). Around  $t \sim 12.5$ , centrifugal force decelerates the radial inflow. The pressure gradient force contributes to turn the direction of motion toward the vertical direction. When the gravitational force becomes zero ( $t \sim 12.8$ ), the pressure gradient force along the streamline reaches maximum, while the centrifugal force still decelerates the particle. At  $t = 13.16$ , the centrifugal barrier finally turns the direction of the motion of the particle to the  $+r$  direction. After the radial velocity becomes positive, centrifugal force and the Lorentz force slowly accelerate the particle along the magnetic field line ( $t > 13.4$ ).

Figure 8 (*left*) shows the trajectories of particles that are initially located on a magnetic field line at  $r = 0.8r_0$  for model I. The initial position of particles is selected such that the particles form the main part of the jet. Figure 8 (*right*) shows the forces along the streamline of the particle denoted by open circles in Figure 8 (*left*). Until  $t \sim 4.6$ , centrifugal force almost balances

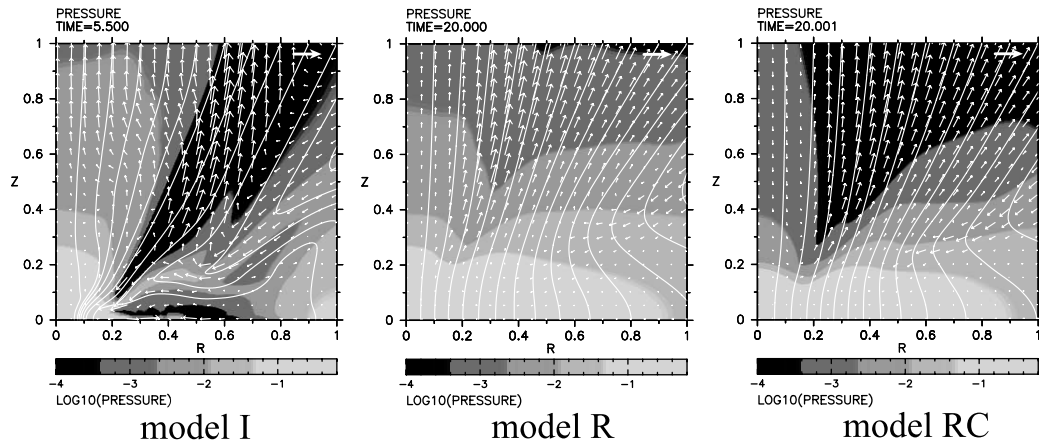


FIG. 4.—Pressure distribution in model I (*left*), model R (*center*), and model RC (*right*). White curves show the magnetic field lines, arrows show the velocity vectors, and the arrow at the upper right corner shows the unit velocity.

with the radial gravity (i.e., Keplerian rotation). Around  $t = 4.85$ , when the particle turns its direction to the  $+r$  direction, the Lorentz force has the largest contribution to the acceleration of the particle. After  $t = 4.9$ , the summation of centrifugal force and the Lorentz force accelerates the particle. This result is consistent with that of Kudoh et al. (1998) and Kato et al. (2002). Since the magnetic forces are much larger than those in model R (Fig. 7), acceleration is larger.

Figure 9 shows the time dependence of the  $r$  and  $z$  components of each force per mass acting on the Lagrangian particle shown as an open circle in Figure 7 (*left*) for model R. The left panels show the  $r$ -component and the right panels show the  $z$ -component. In the radial direction, centrifugal force exceeds the radial gravity around  $t \sim 12$ . Subsequently, the radial com-

ponent of the Lorentz force collimates the outflow ( $t \sim 14$ ). In the vertical direction, the fluid element is lifted almost hydrostatically near the ejection time ( $t \sim 12.5$ ) and subsequently accelerated by the Lorentz force ( $t \sim 14$ ). It means that the centrifugal barrier turns the direction of inflows. At the same time, the vertical component of the pressure gradient force lifts the particle toward the  $z$ -direction and finally it is accelerated by the Lorentz force. Thus, the radial inflow turns into the outflow along the magnetic field line.

Figure 10 (*top*) shows the magnetic pressure  $\log_{10} P_B$  and the gas pressure  $\log_{10} P_g$  along the magnetic field line depicted in Figure 5 (*left*). The vertical dotted lines in the top, middle, and bottom panels of Figure 10 show the ejection point of the jet where  $V_r = 0$ . At the ejection point, the gas pressure is dominant. On the

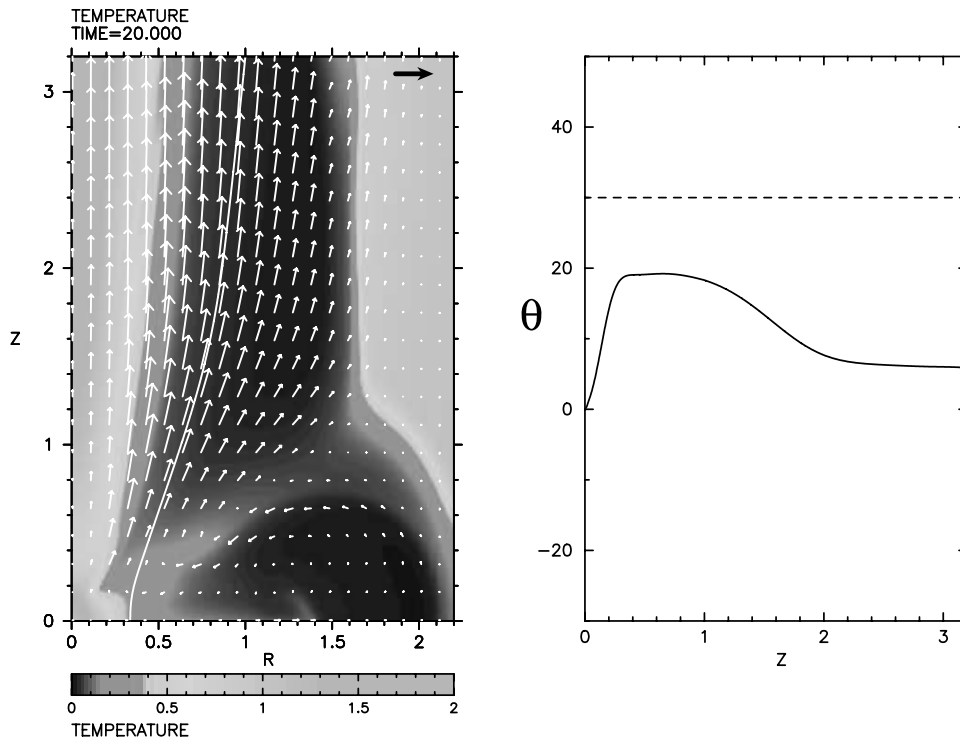


FIG. 5.—*Left*: Temperature distribution at  $t = 20.0$  in model R ( $\bar{\eta} = 1.25 \times 10^{-2}$ ). *Right*: Spatial variation of the angle  $\theta$  between the poloidal magnetic field line depicted in the left panel and the rotational axis as a function of  $z$ . The dashed line shows the critical angle over which the magnetocentrifugal acceleration drives outflows.

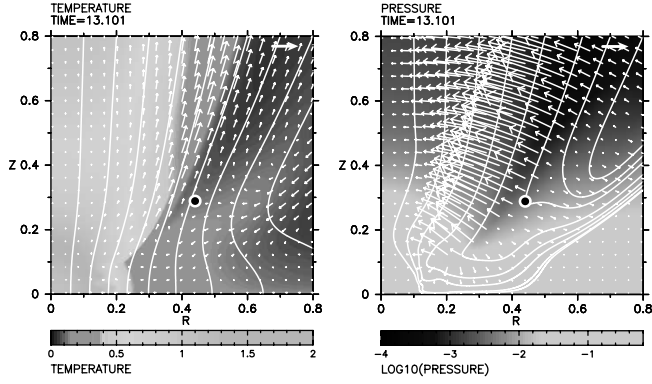


FIG. 6.—Close up of the jet-launching region of model R ( $\bar{\eta} = 1.25 \times 10^{-2}$ ) at  $t = 13.1$ . *Left*: The gray-scale contour shows the temperature distribution, the arrows show the poloidal velocity vectors (an arrow at upper right corner shows the reference velocity vector  $= V_{K0}$ ), and white curves show poloidal magnetic field lines. The black circle shows the position of the Lagrangian particle at this time. *Right*: The gray-scale contour shows the pressure distribution, arrows show the poloidal component of the Lorentz force (an arrow at upper right corner shows the reference vector  $= 3GM/r_0^2$ ), and white curves show poloidal stream lines. The black circle shows the position of the Lagrangian particle at this time.

other hand, the magnetic pressure becomes dominant in  $z > 0.35$ . Figure 10 (*middle*) shows the effective potential,

$$\Psi_{\text{eff}} = -\frac{1}{(r^2 + z^2)^{1/2}} - \frac{1}{2}\Omega^2 r^2, \quad (14)$$

along the magnetic field line shown by a white curve in Figure 5 (*left*). The solid circle shows the slow magnetosonic point where  $V_p = V_{\text{slow}}$ . Here  $V_p$  is the poloidal speed and  $V_{\text{slow}}$  is the slow magnetosonic speed, defined as

$$V_{\text{slow}} = \frac{1}{2} \left[ V_s^2 + V_A^2 - \sqrt{(V_A^2 + V_s^2)^2 - 4V_{p,A}^2 V_s^2} \right], \quad (15)$$

where  $V_{p,A}^2 = B_p^2/(4\pi\rho)$ .

The fluid elements in the region of  $d\Psi_{\text{eff}}/dl < 0$  are accelerated by the magnetocentrifugal force and those in the region of  $d\Psi_{\text{eff}}/dl > 0$  accrete in the case of ideal MHD (Kudoh et al. 1998), where  $l$  is the line element of a magnetic field line. How-

ever, in the resistive model, the gas in the region  $d\Psi_{\text{eff}}/dl > 0$  is ejected because the gradient of gas pressure along a magnetic field line lifts the fluid elements and enables them to jump over the potential barrier. Subsequently, the gas is accelerated by magnetocentrifugal force. On the other hand, in the ideal MHD case the ejection point locates almost at the top of the effective potential ( $d\Psi_{\text{eff}}/dl \sim 0$ ) and the slow magnetosonic point almost coincides with this point (Fig. 10, *bottom*).

### 3.3. Quasi Stationarity of Outflow

Figure 11 (*top*) shows the time evolution of fluxes of angular momentum and mass,

$$F_l = 2 \int_0^{2.5} 2\pi r \left( r\rho V_z V_\phi - \frac{rB_z B_\phi}{4\pi} \right) dr, \quad (16)$$

$$F_m = 2 \int_0^{2.5} 2\pi r \rho V_z dr, \quad (17)$$

at  $z = 3r_0$ . The angular momentum and mass fluxes approach constant values around  $t = 25$ . Figure 11 (*bottom*) shows the distribution of the following quantities on the magnetic field line depicted in Figure 5:

$$K = 4\pi\rho \frac{|V_p|}{|B_p|}, \quad (18)$$

$$\Lambda = rV_\phi - \frac{rB_\phi}{K}, \quad (19)$$

$$\Omega = \frac{V_\phi}{r} - \frac{KB_\phi}{4\pi\rho r}, \quad (20)$$

$$S = \log\left(\frac{P}{\rho^\gamma}\right), \quad (21)$$

$$E = \frac{\gamma P}{(\gamma - 1)\rho} + \psi - \frac{r^2\Omega^2}{2} + \frac{V_p^2}{2} + \frac{r^2(V_\phi/r - \Omega)^2}{2}. \quad (22)$$

In the ideal MHD case, these quantities should be constant along a magnetic field line (Ustyugova et al. 1999). The vertical dotted line shows the position where  $V_r$  is zero (the ejection point of the jet). The quantities are nearly constant even in the

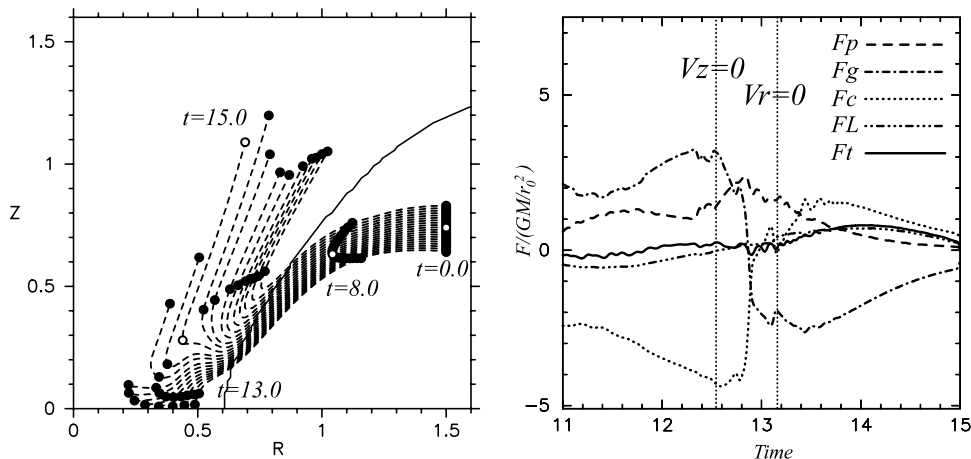


FIG. 7.—*Left*: Trajectories of Lagrangian particles in model R ( $\bar{\eta} = 1.25 \times 10^{-2}$ ). Dashed curves show the trajectories of Lagrangian test particles. The solid curve shows the initial disk surface. Circles are the location of test particles at times denoted in the figure. *Right*: Forces along the streamline of the particle shown by open circles in the left panel. Forces accelerate the particle when the sign is positive and decelerate the particle when the sign is negative. Radial velocity  $V_r$  and vertical velocity  $V_z$  change their sign at the time denoted by vertical dotted lines. Curves  $F_c$ ,  $F_g$ ,  $F_p$ ,  $F_L$ , and  $F_t$  show centrifugal force, gravity, pressure gradient force, poloidal Lorentz force, and total force.

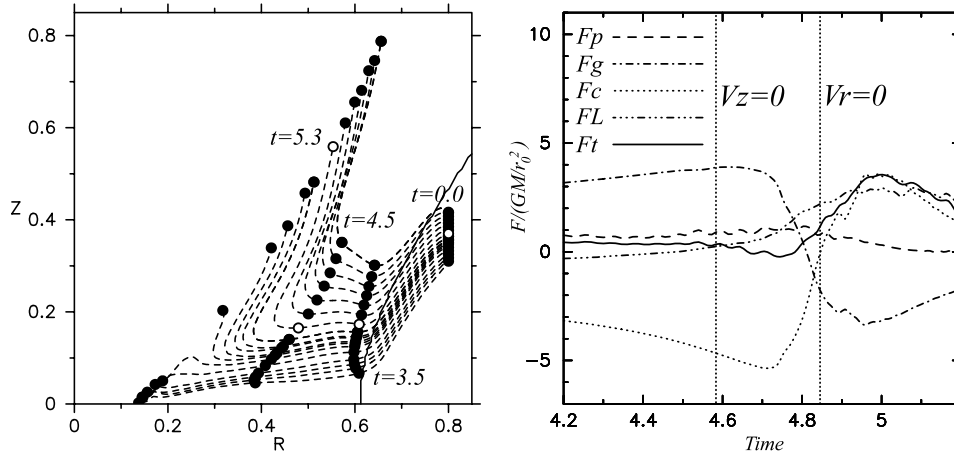


FIG. 8.—*Left*: Trajectories of Lagrangian particles in model I ( $\bar{\eta} = 0.0$ ). Dashed curves show the trajectories of test particles. The solid curve shows the initial disk surface. Circles are the location of test particles at times denoted in the figure. *Right*: Forces along the streamline of the particle shown by open circles in the left panel. Forces accelerate the particle when the sign is positive and decelerate the particle when the sign is negative. Radial velocity  $V_r$  and vertical velocity  $V_z$  change their sign at the time denoted by vertical dotted lines. Curves  $F_c$ ,  $F_g$ ,  $F_p$ ,  $F_L$ , and  $F_t$  show centrifugal force, gravity, pressure gradient force, poloidal Lorentz force, and total force.

resistive model. These results indicate the quasi stationarity of the outflow.

### 3.4. Powers of Jets

To study the energetics of the jet formation and compare them with the results by Casse & Keppens (2004), we compute the energy liberated by accretion  $P_{\text{acc}}$  and the power of jet  $P_{\text{jet}}$ , defined as follows:

$$P_{\text{acc}} = P_{\text{mec}} + P_{\text{ent}} + P_{\text{MHD}}, \quad (23)$$

$$P_{\text{mec}} = -2 \int_0^{0.3} 2\pi r \rho V_r \left( \frac{V^2}{2} + \psi \right) dz, \quad (24)$$

$$P_{\text{ent}} = -2 \int_0^{0.3} 2\pi r \rho V_r \left( \frac{\gamma}{\gamma-1} \frac{P}{\rho} \right) dz, \quad (25)$$

$$P_{\text{MHD}} = -2 \int_0^{0.3} 2\pi r \frac{c}{4\pi} (\mathbf{E} \times \mathbf{B})_r dz, \quad (26)$$

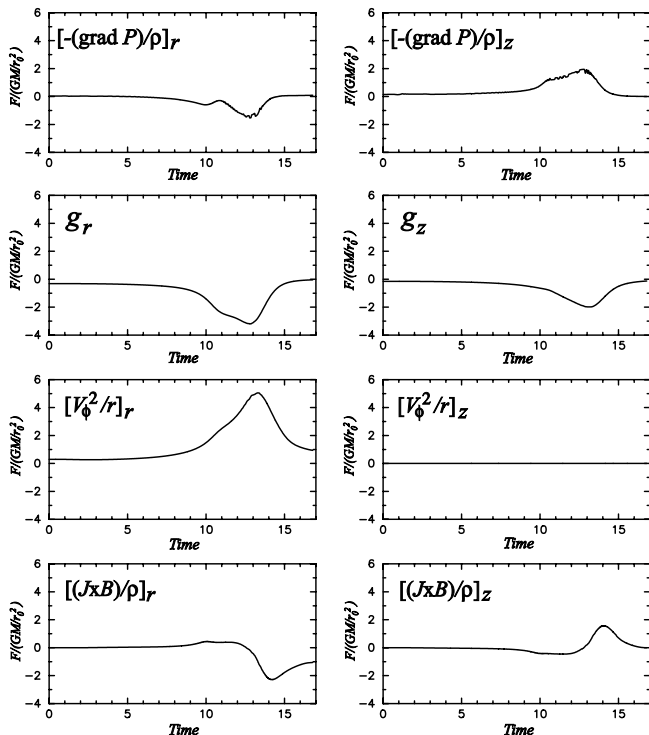


FIG. 9.—Time evolution of  $r$ - and  $z$ -components of each force acting on the Lagrangian particle (open circle) in Fig. 7 (model R).

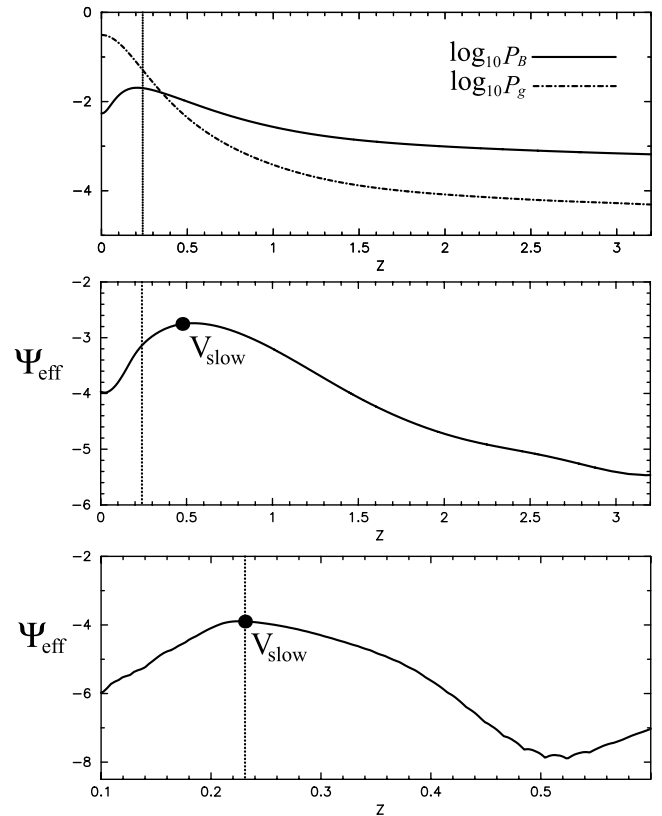


FIG. 10.—*Top*: Distribution of magnetic pressure  $P_B$  and gas pressure  $P_g$  at  $t = 20$  on the magnetic field line depicted in Fig. 5. *Middle*: Distribution of effective potential at  $t = 20$  on the magnetic field line depicted in Fig. 5. *Bottom*: Distribution of effective potential at  $t = 5.5$  along a magnetic field line in the main part of the ideal MHD jet (model I). The vertical dotted line shows the ejection point of the jet ( $V_r > 0$ ). Solid circles show the slow magnetosonic point.

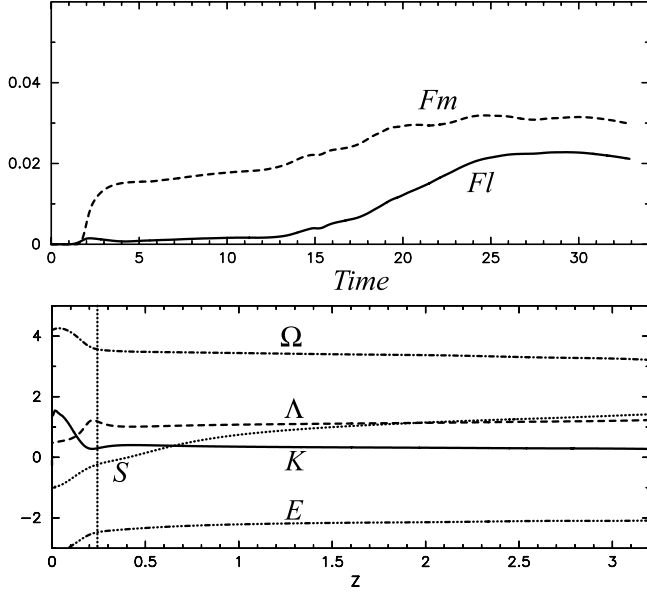


FIG. 11.—*Top*: Time evolution of fluxes of angular momentum  $F_l$  and mass  $F_m$ . *Bottom*: Distribution of variables,  $K = 4\pi\rho|V_p|/|B_p|$ ,  $\Lambda = rV_\phi - rB_\phi/K$ ,  $\Omega = V_\phi/r - KB_\phi/(4\pi\rho r)$ ,  $S = \log(P/\rho^\gamma)$ , and  $E = [\gamma/(\gamma-1)]P/\rho + \psi - \Omega^2 r^2/2 + V_p^2/2 + (V_\phi/r - \Omega)^2 r^2/2$  at  $t = 20$  on the magnetic field line depicted in Fig. 5. The vertical dotted line shows the ejection point of the jet ( $V_r > 0$ ).

at  $r = 0.4r_0$ , and

$$P_{\text{jet}} = P_{\text{mec},J} + P_{\text{ent},J} + P_{\text{MHD},J}, \quad (27)$$

$$P_{\text{mec},J} = 2 \int_0^{2.5} 2\pi r \rho V_z \left( \frac{V^2}{2} + \psi \right) dr, \quad (28)$$

$$P_{\text{ent},J} = 2 \int_0^{2.5} 2\pi r \rho V_z \left( \frac{\gamma}{\gamma-1} \frac{P}{\rho} \right) dr, \quad (29)$$

$$P_{\text{MHD},J} = 2 \int_0^{2.5} 2\pi r \frac{c}{4\pi} (\mathbf{E} \times \mathbf{B})_z dr, \quad (30)$$

at  $z = 3r_0$ .

Figure 12 shows the time evolution of the energy fluxes in the jet: a mechanical power  $P_{\text{mec},J}$ , enthalpy flux  $P_{\text{ent},J}$ , Poynting

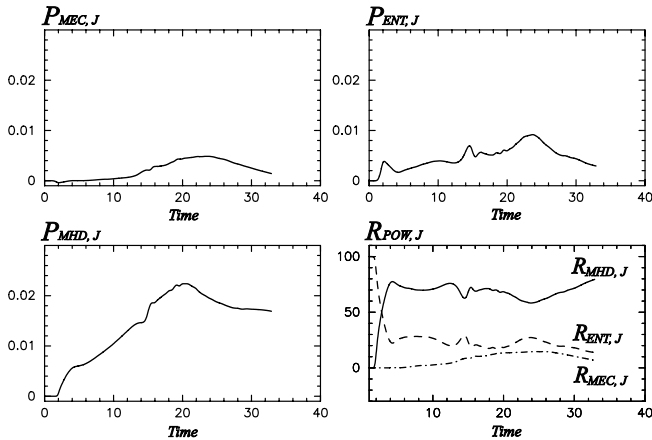


FIG. 12.—Time evolution of powers accelerating the jet; mechanical power  $P_{\text{mec},J}$ , enthalpy  $P_{\text{ent},J}$ , Poynting flux  $P_{\text{MHD},J}$ , and the ratio  $R_{\text{pow},J}$  of each power to total power.  $R_{\text{MHD},J}$ ,  $R_{\text{ent},J}$ , and  $R_{\text{mec},J}$  are the ratio of Poynting flux, enthalpy, and mechanical power to total power of jet.

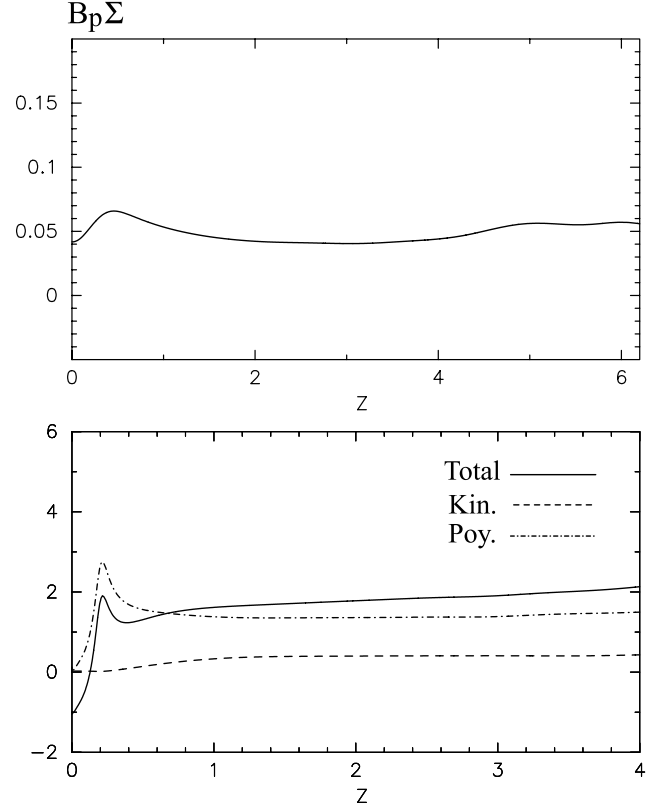


FIG. 13.—*Top*: Magnetic flux  $B_p \Sigma$  at  $t = 20$  along the magnetic field line depicted in Fig. 5;  $\Sigma (\Sigma \propto r^2)$  is a cross section of the flux tube. *Bottom*: Specific energies at  $t = 20$  along the magnetic field line in Fig. 5. The solid curve shows the total energy  $E = V_p^2/2 + V_\phi^2/2 + [\gamma/(\gamma-1)]P/\rho + \psi - r\Omega' B_\phi/(4\pi\lambda')$ , the dashed curve shows the poloidal kinetic energy  $V_p^2/2$ , and the dash-dotted curve shows the Poynting flux divided by  $\rho V_p$ ,  $-r\Omega' B_\phi/(4\pi\lambda')$ .

flux  $P_{\text{MHD},J}$ , and the ratio  $R_{\text{pow},J}$  of each power to the total power  $P_{\text{jet}}$  at  $z = 3$ . The dominant energy flux at this height is the Poynting flux, whose ratio to the total power is  $R_{\text{MHD},J} \sim 70\%$ . The enthalpy flux and the mechanical flux contribute to  $R_{\text{ent},J} \sim 20\%$  and  $R_{\text{mec},J} \sim 10\%$ , respectively.

Kudoh & Shibata (1997) showed that the dominant energy of a jet depends on the strength of the magnetic field. When the poloidal component of the magnetic field is  $B_p \propto r^{-2}$ , the fast magnetosonic point appears far from the Alfvén point and the dominant energy of the jet is the Poynting flux. In our simulations, the initial magnetic field is uniform. In such models, the fast magnetosonic point locates far from the Alfvén point (Kuwabara et al. 2000).

Figure 13 (*top*) shows the magnetic flux  $B_p \Sigma$  along the magnetic field line depicted in Figure 5;  $\Sigma (\Sigma \propto r^2)$  is a cross section of the flux tube. Since  $B_p \Sigma \sim \text{constant}$ ,  $B_p \propto r^{-2}$ . Figure 13 (*bottom*) shows the total specific energy  $E = V_p^2/2 + V_\phi^2/2 + [\gamma/(\gamma-1)]P/\rho + \psi - r\Omega' B_\phi/(4\pi\lambda')$ . Here  $V_p^2/2$  is the poloidal kinetic energy,  $-r\Omega' B_\phi/(4\pi\lambda')$  is the Poynting flux divided by  $\rho V_p$  where  $\Omega' = -V_p B_\phi/B_p + V_\phi/r$ , and  $\lambda' = \rho V_p/B_p$ . Figure 13 shows that the Poynting flux is dominant. It is consistent with the case of  $B_p \propto r^{-2}$  in Kudoh & Shibata (1997).

Figure 14 shows the time evolution of the mechanical power  $P_{\text{mec}}$ , enthalpy flux  $P_{\text{ent}}$ , Poynting flux  $P_{\text{MHD}}$  transported inward through  $r = 0.4r_0$  in the disk, and the ratio of the total power of the jet  $P_{\text{jet}}$  to the total power liberated by accretion  $P_{\text{acc}}$ . Numerical results of model R indicate that  $-P_{\text{ent}}/P_{\text{mec}} \sim 0.4$ ,  $P_{\text{MHD}}/P_{\text{mec}} \sim 0.1$ , and  $P_{\text{acc}}/P_{\text{mec}} \sim 0.7$ . Meanwhile,  $P_{\text{jet}} \sim P_{\text{acc}}$ . Thus,  $\sim 70\%$

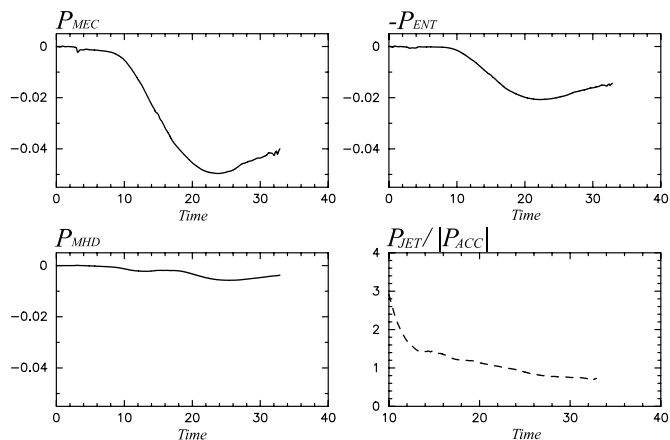


FIG. 14.—Time evolution of powers liberated by accretion, mechanical power  $P_{mec}$ , enthalpy  $P_{ent}$ , Poynting flux  $P_{MHD}$  transported inward through  $r = 0.4r_0$  in the disk, and the ratio of the total power of jet to the total power of accretion  $P_{jet}/|P_{acc}|$ ,  $P_{acc} = P_{mec} + P_{ent} + P_{MHD}$ .

of the mechanical energy released by mass accretion powers the jet.

#### 4. SUMMARY AND DISCUSSION

In this paper, we studied the acceleration mechanism of resistive MHD jets launched from accretion disks threaded by weak large-scale poloidal magnetic fields. We recomputed the models we reported in Kuwabara et al. (2000) by applying the CIP-MOCCT scheme modified for resistive MHD equations. We carried out simulations for a timescale of about 50 times the inner orbital time. Figure 15 shows the ejection mechanism of resistive MHD jets. In mildly resistive disks, the disk gas infalls without losing much of its angular momentum because magnetic field lines are less deformed than those in ideal MHD model. Thus, the matter accreting from the initial torus hits the centrifugal barrier and forms a high-pressure inner disk whose pressure gradient force enables the accreting material to jump over the barrier of the effective potential. The material lifted up by pressure gradient force passes through the slow magnetosonic point and is accelerated by the magnetocentrifugal force. Mass accretion/outflow takes place continuously and the system approaches a quasi-steady inflow-outflow state.

The main acceleration force is the magnetocentrifugal force for both resistive and nonresistive models. The point of acceleration by the magnetocentrifugal force depends on the resistivity and is  $z \sim 0.6r_0$  when  $\bar{\eta} \sim 0.01$  and  $z \sim 0.25r_0$  when  $\bar{\eta} = 0$ . The acceleration force for the resistive model is only 25% of the acceleration for nonresistive case. We confirmed that Joule heating is not essential for the formation of jets.

Through resistive MHD simulations, treating the accretion disk as the fixed boundary, Fendt & Čemeljić (2002) showed that the jet velocity increases with increasing diffusivity. This result is consistent with the result of Kuwabara et al. (2000) that the mass outflow rate increases with the resistivity up to some critical value. The timescale approaching the quasi-steady state is shorter in our approach, which includes the disk in the simulation region because accretion of the disk material deforms the magnetic field lines.

Casse & Keppens (2004) showed by MHD simulations assuming the magnetic diffusivity localized inside the disk that

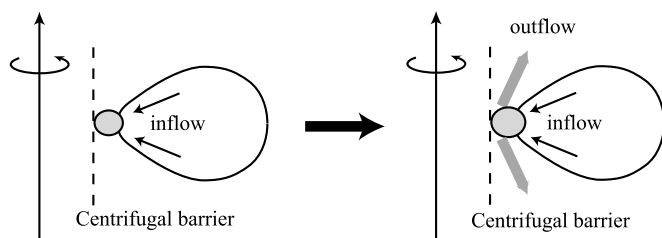


FIG. 15.—Schematic picture of the ejection mechanism of the outflow in model R ( $\bar{\eta} = 1.25 \times 10^{-2}$ ). The gray region shows the high-pressure inner torus created by the adiabatic compression of gases.

resistive MHD jets are formed from a thin disk threaded by global poloidal magnetic fields. Although the initial conditions and model parameters of our simulations are quite different from those of Casse & Keppens, the density distribution and structures of magnetic field lines of the disk-jet system at the final quasi-steady state are similar (see Fig. 2 of Casse & Keppens 2004).

The energy flux of jets in our mildly resistive model is mainly transported by the Poynting flux, while the mechanical flux dominates the outflow in Casse & Keppens (2004). Kudoh & Shibata (1997) showed that the dominant energy of a jet depends on the strength of the magnetic field. When the poloidal component of magnetic field is  $B_p \propto r^{-2}$ , the fast magnetosonic point appears far from the Alfvén point and the dominant energy of the jet is Poynting flux. When  $B_p \propto r^{-(2+a)}$  where  $a > 0$ , the fast magnetosonic point locates near the Alfvén point and the dominant energy is the kinetic energy. In our model,  $B_p$  is constant with radius at the initial state. Numerical results are consistent with those in Kudoh & Shibata (1997) when  $B_p$  decreases slowly with radius. Since magnetic energy decreases faster in Casse & Keppens (2004), the fast magnetosonic point locates closer to the ejection point of the jet. Thus, in Casse & Keppens (2004), the jet is dominated by kinetic energy.

The jet power ( $P_{jet}$ ) is comparable to the energy released by mass accretion ( $P_{acc}$ ), which is  $\sim 70\%$  of the released mechanical energy  $P_{mec}$ . As Casse & Keppens (2004) pointed out, in ADAF (advection dominated accretion flows),  $P_{mec} \sim -P_{ent}$  so that  $P_{acc} \sim 0$ . Thus, the resistive inflow-outflow configuration is different from ADAF. Our numerical results can be interpreted as magnetic analogue of advection dominated inflow-outflow solutions (ADIOS) that appears in hydrodynamic models with high phenomenological viscosity (Blandford & Begelman 1999).

We thank Seiichi Kato for helping us to extract forces acting on particles. This work was supported by the Japan Society for the Promotion of Science Japan-UK Cooperation Science Program (principal investigators: K. Shibata and N. O. Weiss), the Astronomical Data Analysis Center of the National Astronomical Observatory, Japan, the ACT-JST of Japan Science and Technology Corporation, and the National Science Council, Taiwan, under the grants NSC-90-2811-M-008-020, NSC-91-2112-M-008-006. The numerical computations were carried out on VPP5000 at the Astronomical Data Analysis Center of the National Astronomical Observatory, Japan, under the projects rmh17b and rhn31b.

## REFERENCES

- Abramowicz, M., Jaroszynski, M., & Sikora, M. 1978, *A&A*, 63, 221  
Balbus, S. A., & Hawley, J. F. 1991, *ApJ*, 376, 214  
Blandford, R. D., & Begelman, M. C. 1999, *MNRAS*, 303, L1  
Blandford, R. D., & Payne, D. G. 1982, *MNRAS*, 199, 883  
Casse, F., & Keppens, R. 2002, *ApJ*, 581, 988  
———. 2004, *ApJ*, 601, 90  
Fendt, C., & Čemeljić, M. 2002, *A&A*, 395, 1045  
Galeev, A. A., Rosner, R., Serio, S., & Vaiana, S. 1981, *ApJ*, 243, 301  
Kato, S. X., Kudoh, T., & Shibata, K. 2002, *ApJ*, 565, 1035  
Kudoh, T., Matsumoto, R., & Shibata, K. 1998, *ApJ*, 508, 186  
———. 1999, *J. Comput. Fluid Dyn.*, 8, 56  
———. 2002, *PASJ*, 54, 121  
Kudoh, T., & Shibata, K. 1997, *ApJ*, 474, 362  
Kuwabara, T., Shibata, K., Kudoh, T., & Matsumoto, R. 2000, *PASJ*, 52, 1109  
Matsumoto, R., Uchida, Y., Hirose, S., Shibata, K., Hayashi, M. R., Ferrari, A., Bodo, G., & Norman, C. 1996, *ApJ*, 461, 115  
Ouyed, R., & Pudritz, R. E. 1997, *ApJ*, 482, 712  
Romanova, M. M., Ustyugova, G. V., Koldoba, A. V., Chechetkin, V. M., & Lovelace, R. V. E. 1997, *ApJ*, 482, 708  
Shibata, K., & Uchida, Y. 1986, *PASJ*, 38, 631  
Stone, J. M., & Norman, M. L. 1992, *ApJS*, 80, 753  
———. 1994, *ApJ*, 433, 746  
Uchida, Y., & Shibata, K. 1985, *PASJ*, 37, 515  
Ustyugova, G. V., Koldoba, A. V., Romanova, M. M., Chechetkin, V. M., & Lovelace, R. V. E. 1995, *ApJ*, 439, L39  
———. 1999, *ApJ*, 516, 221  
Yabe, T., & Aoki, T. 1991, *Comp. Phys. Comm.*, 66, 219